



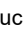







RESEARCH ARTICLE | OCTOBER 18 2023

# Composition variations in $\text{Cu}(\text{In,Ga})(\text{S,Se})_2$ solar cells: Not a gradient, but an interlaced network of two phases

Aubin JC. M. Prot ; Michele Melchiorre ; Felix Dingwell; Anastasia Zelenina; Hossam Elanzeery ; Alberto Lomuscio; Thomas Dalibor ; Maxim Guc ; Robert Fonoll-Rubio ; Victor Izquierdo-Roca ; Gunnar Kusch ; Rachel A. Oliver ; Susanne Siebentritt 



APL Mater. 11, 101120 (2023)

<https://doi.org/10.1063/5.0165546>



CrossMark

## Articles You May Be Interested In

Completing the dark matter solutions in degenerate Kaluza-Klein theory


*J. Math. Phys.* (April 2019)

Gibbs measures based on 1d (an)harmonic oscillators as mean-field limits

*J. Math. Phys.* (April 2018)

An upper diameter bound for compact Ricci solitons with application to the Hitchin–Thorpe inequality. II

*J. Math. Phys.* (April 2018)



THE ADVANCED MATERIALS MANUFACTURER®

yttrium iron garnet    glassy carbon    beamsplitters    fused quartz    additive manufacturing

zeolites    III-IV semiconductors    gallium lump    copper nanoparticles    organometallics

nano ribbons    barium fluoride    europium phosphors    photonics    infrared dyes

sapphire windows    Nd:YAG    epitaxial crystal growth    ultra high purity materials    transparent ceramics    CIGS

spintronics    raman substrates    cerium oxide polishing powder    cermet    nanodispersions

silver nanoparticles    perovskites    surface functionalized nanoparticles    MBE grade materials    thin film

MOCVD    beta-barium borate    sputtering targets    fiber optics

rare earth metals    quantum dots    h-BN    deposition slugs

osmium    scintillation Ce:YAG    CVD precursors    photovoltaics

refractory metals    laser crystals    metamaterials    borosilicate glass

antiferromagnetic films    niobate    InAs wafers    YBCO    superconductors    InGaAs

MOFs    AuNPs    ZnS    CdTe    indium tin oxide    MgF<sub>2</sub>    rutile    optical glass

perovskite crystals    transparent ceramics    diamond micropowder

**Now Invent.™**

[www.americanelements.com](http://www.americanelements.com)

© 2001-2023, American Elements Inc. a U.S. Registered Trademark

# Composition variations in $\text{Cu}(\text{In,Ga})(\text{S,Se})_2$ solar cells: Not a gradient, but an interlaced network of two phases

Cite as: APL Mater. 11, 101120 (2023); doi: 10.1063/5.0165546

Submitted: 29 June 2023 • Accepted: 3 October 2023 •

Published Online: 18 October 2023



Aubin JC. M. Prot,<sup>1,a)</sup> Michele Melchiorre,<sup>1</sup> Felix Dingwell,<sup>1</sup> Anastasia Zelenina,<sup>2</sup> Hossam Elanzeery,<sup>2</sup> Alberto Lomuscio,<sup>2</sup> Thomas Dalibor,<sup>2</sup> Maxim Guc,<sup>3</sup> Robert Fonoll-Rubio,<sup>3</sup> Victor Izquierdo-Roca,<sup>3</sup> Gunnar Kusch,<sup>4</sup> Rachel A. Oliver,<sup>4</sup> and Susanne Siebentritt<sup>1</sup>

## AFFILIATIONS

<sup>1</sup>Laboratory for Photovoltaics, Physics and Materials Science Research Unit, University of Luxembourg, 41 rue du Brill, Belvaux L-4422, Luxembourg

<sup>2</sup>AVANCIS GmbH, Otto-Hahn-Ring 6, 81739 München, Germany

<sup>3</sup>Catalonia Institute for Energy Research (IREC), Jardins de les Dones de Negre 1, 2a pl., 08930 Sant Adrià de Besòs, Barcelona, Spain

<sup>4</sup>Department of Materials Science and Metallurgy, University of Cambridge, 27 Charles Babbage Road, Cambridge CB3 0FS, United Kingdom

<sup>a)</sup>Author to whom correspondence should be addressed: [aubin.prot@uni.lu](mailto:aubin.prot@uni.lu)

## ABSTRACT

Record efficiency in chalcopyrite-based solar cells  $\text{Cu}(\text{In,Ga})(\text{S,Se})_2$  is achieved using a gallium gradient to increase the bandgap of the absorber toward the back side. Although this structure has successfully reduced recombination at the back contact, we demonstrate that in industrial absorbers grown in the pilot line of Avancis, the back part is a source of non-radiative recombination. Depth-resolved photoluminescence (PL) measurements reveal two main radiative recombination paths at 1.04 eV and 1.5–1.6 eV, attributed to two phases of low and high bandgap material, respectively. Instead of a continuous change in the bandgap throughout the thickness of the absorber, we propose a model where discrete bandgap phases interlace, creating an apparent gradient. Cathodoluminescence and Raman scattering spectroscopy confirm this result. Additionally, deep defects associated with the high gap phase reduce the absorber's performance. Etching away the back part of the absorber leads to an increase of one order of magnitude in the PL intensity, i.e., 60 meV in quasi-Fermi level splitting. Non-radiative voltage losses correlate linearly with the relative contribution of the high energy PL peak, suggesting that reducing the high gap phase could increase the open circuit voltage by up to 180 mV.

© 2023 Author(s). All article content, except where otherwise noted, is licensed under a Creative Commons Attribution (CC BY) license (<http://creativecommons.org/licenses/by/4.0/>). <https://doi.org/10.1063/5.0165546>

## I. INTRODUCTION

Thin film solar modules based on  $\text{Cu}(\text{In,Ga})(\text{S,Se})_2$  (CIGSSe) absorbers are already used in large scale production; AVANCIS/CNBM has a nominal production capacity of more than 1 GW. They reach a record power conversion efficiency (PCE) of 20.3% for  $30 \times 30 \text{ cm}^2$  submodules<sup>1</sup> and of 23.6% for cells.<sup>2</sup> The previous cell record of 23.4%<sup>3</sup> as well as the current submodule record make use of a double graded band profile. The front surface gradient is achieved by increasing the sulfur content at the front, while the back

surface gradient arises from a higher gallium content at the back of the absorber. Variation of the  $\text{Ga}/(\text{Ga} + \text{In})$  ratio (GGI) over the thickness of the absorber has been studied for years. The resulting increasing bandgap gradient toward the back side has been proven to help drive the carriers away from the back contact, thus preventing them from recombining non-radiatively before collection.<sup>4–7</sup>

Understanding the recombination activity in solar cells is essential, as non-radiative recombinations reduce the efficiency of the device. Carriers generated in the active material can either recombine radiatively by emitting a photon with the energy of

the transition or non-radiatively, losing the energy to the lattice. In their famous publication on efficiency limits,<sup>8</sup> Shockley and Queisser already addressed the impact of non-radiative recombinations, demonstrating their detrimental effect on cell performance. A measure of the radiative recombinations and, by extension, of the non-radiative processes is given by the photoluminescence quantum yield (PLQY,  $f_c$  in the Shockley–Queisser paper), i.e., the ratio of the emitted photon flux over the incoming photon flux in a photoluminescence (PL) experiment. PL spectroscopy is a powerful and well known tool that can be used at an early stage in the preparation of solar cells to obtain valuable information about the quality of the absorber layer itself.<sup>9</sup> The current highest PLQY of a solar cell is obtained for GaAs cells, reaching 35.7%, whereas chalcopyrite based solar cells typically perform in the range of 0.1%–1%.<sup>10</sup>

All the absorbers investigated in this study are grown in the pilot line of AVANCIS, Germany.<sup>11,12</sup> They present an intentional double bandgap gradient toward the front and back sides, induced by a sulfur and a gallium gradient, respectively. In this work, we compare the recombination activity from the front and back sides of these industrial Cu(In,Ga)(S,Se)<sub>2</sub> absorbers. We show by PL investigation that in graded absorbers, although the minimum of the bandgap, i.e., the notch, dominates the recombination,<sup>13</sup> there is an additional radiative recombination channel visible from the back of the absorbers. We propose here that the GGI does not gradually increase toward the back side as suggested by compositional profiles from Glow Discharge Optical Emission Spectroscopy (GDOES) measurements, but rather that two distinct phases coexist in the bulk of the absorber. A high density of high (low) GGI grains forms at the back (front) of the absorber and becomes sparser at intermediate depth, where the two phases interlace. This leads to an apparent GGI gradient from a compositional point of view. We show further evidence supporting this hypothesis through cathodoluminescence spectroscopy and Raman spectroscopy.

## II. METHODS

### A. Sample preparation

All the absorbers investigated in this study are based on a double barrier back-electrode for the control of alkali-diffusion and Mo selenization. They are grown in the pilot line of AVANCIS, Germany, according to the SEL-RTP process, i.e., a stacked elemental layer followed by rapid thermal processing.<sup>11</sup> The stacked elemental layer consists of precursors of Cu–In–Ga:Na deposited by sputtering and Se thermally evaporated. During the rapid thermal process in sulfur containing atmosphere, this layer reacts to form the CIGS<sub>Se</sub> absorber. The samples used in this study, all grown Cu-poor [with relative comparison summarized in Fig. 1(b)], differ mostly for the In/Ga relative content during the precursor deposition, which consequently changes the overall GGI of the final absorbers, hence also the GGI at their back. Few absorbers have been finished in solar cells and yield an efficiency as high as 17.63% after deposition of anti-reflection coating and light soaking ( $V_{OC}$  = 664 mV,  $J_{SC}$  = 36.77 mA/cm<sup>2</sup>, FF = 72.18%).

### B. Lift-off procedure

To gain direct access to the back side of the absorbers, a lift-off procedure is performed, removing the CIGS<sub>Se</sub> film from its

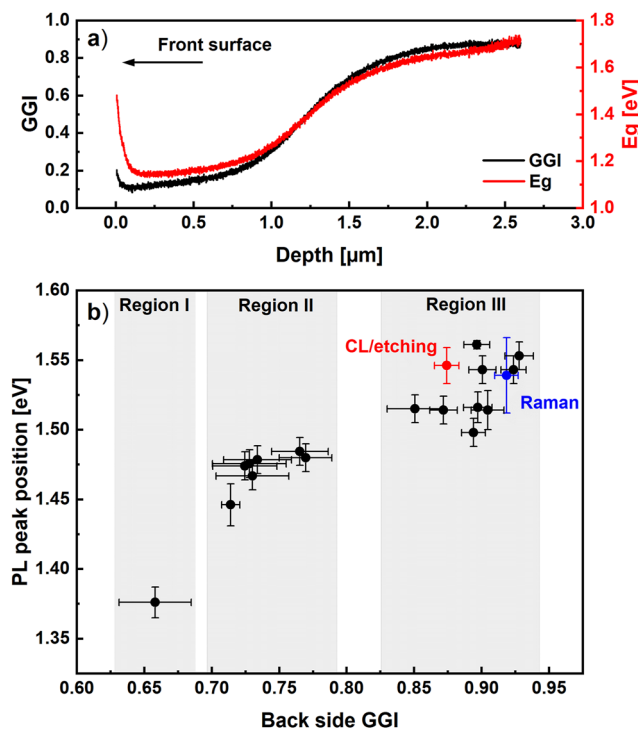


**FIG. 1.** (a) Typical GGI (black) and bandgap (red) profiles of an absorber from region III (red dot) determined from GDOES compositional measurements. The investigated absorbers are all about 2.6  $\mu\text{m}$  thick. The stronger increase of the bandgap from GDOES toward the front is due to the sulfur content, which is higher near the front. (b) 19 samples are investigated. For each of them, the position of the high energy peak is measured by PL from the back side. The error in PL energy is due to inhomogeneities and is determined from different measurements on the same sample. The back side GGI is determined from an average over the last 400 nm of the corresponding GDOES GGI profile. The standard deviation is taken as the error. The two highlighted samples are discussed later in the text.

molybdenum back contact (see Fig. 2). A two-component epoxy glue (Loctite EA 3421) is spread on the front surface of the sample before a clean glass is pressed on it. The glue does not add a luminescence signal in the investigated spectral region. After at least 24 h of curing, the samples are mechanically removed from their substrate by applying some force to them. We found that a short dip of the stack in liquid nitrogen (5–10 s) beforehand helps lift off the film more easily. It has been reported in the literature that the cleavage of such a stack happens at the interface CIGS<sub>Se</sub>/Mo or within the Mo(S<sub>x</sub>Se<sub>y</sub>) layer that forms at the interface.<sup>14–16</sup> X-ray diffraction (XRD) measurement on the remaining substrate—after lift-off—indicates that some residual traces of the CIGS<sub>Se</sub> phase are present, suggesting that the current procedure does not provide an excellent detachment of CIGS<sub>Se</sub> from the Mo layer.

### C. Bromine etching

In order to investigate the absorbers via photoluminescence at different depths, we developed a bromine etching routine to etch part of the absorbers prior to the PL measurement. An aqueous

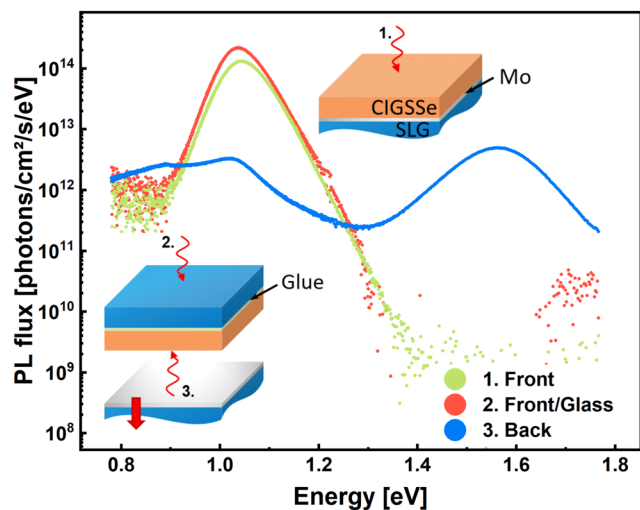


**FIG. 2.** Semi-log scale—absolute photoluminescence spectroscopy at the different stages of the lift-off process: under front side illumination before (1) and after (2) lift-off, respectively, and under back side illumination after lift-off (3). Spectrum 2 has been corrected for the glass emission as indicated in Sec. II.

bromine solution of concentration 0.1 M is prepared by diluting liquid bromine ( $\text{Br}_2$ ) (0.3 ml) into distilled water (60 ml) and finally adding potassium bromide (KBr). The absorbers are dipped into the etching solution for 40 s to 4 min depending on the desired etching depth. The remaining thickness of the etched absorbers is measured by cross-sectional SEM imaging. The etching is either performed on absorbers before the lift-off to remove the front part of the absorber, i.e., the low GGI area, or performed after the lift-off to remove the back part, i.e., the higher GGI area.

#### D. Photoluminescence spectroscopy

We perform absolute calibrated PL measurements, exciting the samples with a 660 nm wavelength diode laser. Achieving the calibration is performed in two steps: spectral correction of the measurements and calibration of the intensity. To fulfill the first point, a commercial halogen lamp of known emission (Avantes AvaLight-HAL-CAL-Mini) is directed onto a Spectralon placed at the sample position, and its spectrum is measured. Comparing the measurement and the calibrated spectrum provided by the company leads to a correction function that takes into account the spectral dependency of the collection system. The second point of calibration requires, on the one hand, measuring the beam radius and laser power at the sample position and computing the resulting expected flux, and on the other hand, measuring its spectrum via the collection system. Comparing the measured (and spectrally corrected) flux with the expected one returns an intensity correction factor. If not specified otherwise in the text, the laser output power is set in such a way that the impinging photon flux is  $2.9 \times 10^{17}$  photons/cm<sup>2</sup>/s, corresponding to one sun generation for a material of bandgap 1.04 eV, based on the AM1.5 solar spectrum. The emission of the sample is directed into an Andor Shamrock sr-303i spectrograph via two parabolic mirrors that focus the emitted photons into an optical

fiber (0.22NA, 550  $\mu\text{m}$  diameter) and is finally detected by a CCD Si camera (Andor iDus DV420A-OE) in the visible range and a CCD InGaAs camera (Andor iDus DU490A-1.7) in the NIR range. For low temperature measurements, the samples are placed in an Oxford Instruments cryostat (OptistatCF) and cooled down to temperatures as low as 10 K using liquid helium as a cryogenic agent. Some samples require being measured through the glass. However, excited with a 660 nm laser, glass emits radiation at 1.5 eV, which adds an unwanted contribution to the PL spectra. Therefore, a preliminary measurement of the glass emission alone is required and can be subtracted from the absorber spectrum (see Fig. S1 in the supplementary material).

#### E. Glow discharge optical emission spectroscopy

Depth profile analysis by Glow Discharge Optical Emission Spectroscopy (GDOES) was applied to evaluate the chemical composition within the CIGS<sub>2</sub> absorbers. The system uses an Ar-plasma for sputtering and a CCD-array to detect the photons emitted during the relaxation of the sputtered and in the plasma excited atoms and ions. All GDOES depth profiles were measured using a GDA 650 HR, a system built by Spectrums Analytik in DC excitation mode (constant voltage-constant current mode) including an anode with an inner diameter of 2.5 mm, corresponding to the actual measurement diameter. The excitation parameters were set to 1000 V and 12 mA. The WinGDOES software was applied to automatically determine quantitative depth profiles of mass concentration and then correct the data with a calibration method developed internally.

#### F. Raman spectroscopy

Raman spectroscopy measurements are performed in a backscattering configuration through a probe designed at IREC using 442, 532, and 785 nm excitation wavelengths. For the 532 and 785 nm excitation wavelengths, the measurement spot diameter is  $\sim 70 \mu\text{m}$  (macro-Raman), and up to 25 points were measured over the entire surface of both the front and back sides, which provided representative information for the whole sample. For the 442 nm excitation wavelength, the measurement spot diameter is  $\sim 2 \mu\text{m}$  (micro-Raman), and 64 points are measured on a  $3 \times 3 \text{ mm}^2$  area from the back side. This allows us to evaluate the inhomogeneities at the micro-scale and acquire information from individual grains. For the 442 and 532 nm excitation wavelengths, a fHR 640 monochromator from Horiba Jobin Yvon, coupled with a CCD detector cooled down to  $-130^\circ \text{C}$ , is used. For the 785 nm excitation wavelength, an iHR 320 monochromator from Horiba Jobin Yvon, coupled with a CCD detector cooled down to  $-70^\circ \text{C}$ , is used. To avoid the presence of thermal effects in the spectra, the excitation power density is kept below  $50 \text{ W}\cdot\text{cm}^{-2}$  in the laser spot. All spectra are calibrated by measuring a reference monocrystalline silicon sample and imposing its main Raman peak at  $520 \text{ cm}^{-1}$ .

#### G. Cathodoluminescence spectroscopy

CL hyperspectral mapping is performed at 300 K on a cleaved cross-section in an Attolight Allalin 4027 Chronos SEM-CL system. CL measurements are taken using an iHR320 spectrometer with a grating density of 150 lines per mm blazed at 500 nm. The



microscope is operated at an electron beam current of 10 nA and an acceleration voltage of 8 kV. The CL hyperspectral maps are then analyzed using LumiSpy.<sup>17</sup>

### III. RESULTS AND DISCUSSION

The composition profile of the studied absorbers is obtained by means of GDOES, from which bandgap profiles can be computed according to Bär *et al.*<sup>18</sup> The typical bandgap and GGI profiles of the absorbers from this study are plotted in Fig. 1(a). As can be observed, gallium accumulates at the back of the absorber, generating the bandgap gradient toward the back. The increase in GGI over the first 100 nm is actually due to a decrease in the indium content in this region rather than an increase in gallium. This feature is particularly pronounced in the absorber shown in Fig. 1(a). The origin of the indium decrease is not yet fully understood.

We empirically observe that the minimum of the bandgap energy ( $E_{g,min}$ ) given by the GDOES profile systematically leads to higher values compared to other measurement methods. Comparing  $E_{g,min}$  of the studied absorbers (see Fig. S2 in supplementary material) obtained from reflection, PL, EQE, and GDOES analysis<sup>9,18–21</sup> reveals that the first three methods agree on  $E_{g,min}$ , whereas GDOES overestimates it by about 55 meV. We believe the reason for this is that not all of the sulfur is incorporated in the grains and that non-negligible amounts of it are located at the grain boundaries. Keller *et al.* investigate the atomic structure around grain boundaries in AVANCIS' CIGSs absorbers by Atom Probe Tomography (APT) and show that sulfur tends to agglomerate at the grain boundaries.<sup>22</sup> Consequently, bandgap energies calculated from composition alone are overestimated due to the apparent higher sulfur content. Additionally, as will be discussed in further detail later, Raman spectroscopy reveals some sulfur-free areas on the back side. Therefore, we will only consider the bandgap profiles in a qualitative way or refer directly to the GGI profiles.

#### A. A high energy peak in the photoluminescence spectra

In order to investigate the recombination activity from the back side of the different samples, the absorber is mechanically removed from its substrate, as described in the methods section, and a subsequent analysis of the PL response from the different faces is conducted. PL spectra measured from the back side show two main emission peaks: one peak centered around 1.03 eV and another peak in the range of 1.5–1.6 eV (see blue spectrum in Fig. 2). The small sharp peak at 0.89 eV is attributed to water absorption,<sup>23</sup> and there is a second broader contribution centered around 0.9 eV that will be discussed in further detail later. The full width half maximum measured for the low energy peak is about 80–90 meV and about 160–180 meV for the high energy peak, observed from the back side. These values are typical of CIGS films.<sup>24</sup>

At room temperature, however, measurements with illumination from the front side before or after the lift-off (red and green spectra in Fig. 2) reveal only one single contribution at about 1.04 eV. This PL emission peak corresponds to band-to-band recombination in the region of the bandgap minimum of the absorber.<sup>9,13</sup>

We therefore argue that from both front and back side illumination, significant recombination originates from the bandgap notch. After the lift-off, the stress applied to the lattice by the molybdenum is released, allowing the lattice to relax. Therefore, we generally observe that the notch PL peak is 10–20 meV lower after lift-off than before, depending on the curing time.<sup>13</sup> The longer the glue cures before the lift-off, the less shift is observed. Moreover, as shown in Fig. 2, the notch luminescence is about two orders of magnitude lower when excited and measured from the back side than from the front side as a consequence of the second recombination channel. According to the bandgap profile shown in Fig. 1, one would expect a higher band-to-band emission while measuring from the back side. However, this model cannot explain why only two peaks are detected. If one assumes that the high energy peak originates from the bandgap gradient at the back side, then all the intermediate band gaps should also be visible by PL and result in one single very broad peak. Unexpectedly, the high energy peak can be detected from the front side as well, but only at low temperatures (in the range of 10–80 K; see Fig. S3 in the supplementary material). At low temperatures, a decrease in the photogenerated carriers' mobility is expected and, therefore, the recombination is more likely to occur at the generation site. Moreover, the absorbers are excited by a laser of wavelength 660 nm with a penetration depth in the material of about 100 nm. It suggests that within the first few hundreds of nanometers from the front surface, the second recombination channel already exists, emitting at 1.5–1.6 eV.

In order to understand the origin of the high energy peak, we prepared a series of absorbers with varying GGI on the back side. As discussed earlier, we believe that the sulfur is not entirely incorporated in the grains and, therefore, we use the back side GGI as a guide to compare the bandgap energy trends between the samples. Note that this does not provide an exact value for the expected band gaps. Figure 1(b) shows the relation between the position of the high energy PL peak measured from the back side and the back side GGI averaged over the last 400 nm of the GDOES profiles. Samples in region III present small changes in the back side GGI, ranging from 0.85 to 0.93, and only a loose correlation is observed for the corresponding high energy PL peak, which varies from 1.50 to 1.56 eV. Samples in region II have a significantly reduced back side GGI of 0.71–0.77. The same PL peak energy is observed within errors, except for one sample with slightly lower peak energy (and lower back side GGI). Finally, the sample in region I has the lowest back side GGI (0.66) and shows the lowest peak energy (1.38 eV). This demonstrates that the bandgap of the high gap phase strongly depends on the GGI at the back side of the absorber.

Based on these results, we argue that there is no continuum of band gaps through the material, as suggested by the GDOES profile in Fig. 1(a), but rather that there are distinct phases of discrete band gaps coexisting throughout the whole thickness of the material. Moreover, the position of the high energy PL peak depends on the gallium content at the very back of the absorbers.

In a previous study on co-evaporated CIGSe absorbers from ZSW, Wolter *et al.* detected a similar high energy peak in addition to the notch peak when measuring from the back side.<sup>13</sup> These samples were grown with a back side GGI of about 0.6, and the high energy peak was detected at 1.31 eV, correlating with the trend observed in this work.

## B. Distinct phases of discrete band gaps

Investigation by Raman spectroscopy of both the front and back sides of the absorbers is conducted to assess whether the different phases are due to different CIGS<sub>Se</sub> compositions or secondary phases. In addition, cross-sectional cathodoluminescence provides local information about the bandgap throughout the film thickness.

Raman spectroscopy measurements are performed under a 532 nm laser excitation in a macro configuration (see methods section for details). This excitation wavelength is close to the bandgap of pure CuGaS<sub>2</sub>,<sup>25</sup> which leads to resonant Raman scattering and a strong increase in the LO components of the polar E/B symmetry modes.<sup>26</sup> Although four absorbers were measured [all from region III in Fig. 1(b)], Fig. 3(a) only shows the normalized Raman spectrum of one of them, as no significant differences could be observed between the samples [blue dot in Fig. 1(b)]. The main peaks, observed at the front side, are associated with the A-like symmetry modes, i.e., Se–Se and S–S vibrations at 178 and 288 cm<sup>−1</sup>, respectively.<sup>27,28</sup> When measuring from the back side, a slight blueshift of these peaks to 185 and 307 cm<sup>−1</sup>, respectively, is observed [see Fig. 3(b)]. This can be explained by the increase in sulfur and gallium content toward the back of the absorbers.<sup>27,29</sup> The associated increase in the bandgap also leads to resonant behavior of the spectra measured from the back side, with a high relative intensity of the LO components of the E/B-like symmetry modes [indicated by the green dashed lines in Figs. 3(a) and 3(b)]. The peaks marked by the gray dashed lines at 170, 238, and 252 cm<sup>−1</sup> are attributed to a MoSe<sub>2</sub> phase detected at the back side of the absorbers.<sup>30</sup> This is an expected secondary phase at the Mo–CIGS<sub>Se</sub> interface. All other peaks are due to CIGS<sub>Se</sub> phases; no additional secondary phases are observed. An investigation of the remaining substrate after lift-off reveals some traces of CIGS<sub>Se</sub> phases, indicating the imperfect removal of the absorber from its substrate.

Additionally, a small peak of an ordered vacancy compound (OVC) phase is visible from both sides, appearing as a shoulder

on the low frequency side of the Se–Se peak, as highlighted in Fig. 3(a) and 3(b) by the red dashed lines.<sup>31</sup> Under the excitation of a 785 nm laser, more of the OVC phase peaks are detected (see Fig. S4 in the supplementary material) from both the front and back sides due to this wavelength being close to resonance for the CuIn<sub>3</sub>Se<sub>5</sub> OVC phase.<sup>32</sup> In Cu-poor chalcopyrites, the formation of off-stoichiometry compounds, i.e., OVCs, is often observed, such as CuIn<sub>3</sub>Se<sub>5</sub> or CuIn<sub>5</sub>Se<sub>8</sub> phases, for instance, in selenide absorbers.<sup>33,34</sup>

Furthermore, the pale lines in Figs. 3(a) and 3(b) represent individual measurements performed at different positions on the absorber. They can be used as an indication of the lateral homogeneity, in terms of chemical composition, of the absorbers' surfaces. Consequently, absorbers are very homogeneous from the front side, whereas significant variation is observed between the individual measurements from the back side, suggesting larger inhomogeneities. In particular, as it can be concluded from the absence of the 307 cm<sup>−1</sup> peak in Fig. 3(c), some sulfur-free areas are present on the back side. More interestingly, grains with significantly different gallium amounts can be detected. The back side of the absorber studied in Fig. 3(a) and 3(b) is additionally scanned over an area of 3 × 3 mm<sup>2</sup> with a 442 nm wavelength laser in micro configuration (see methods section), which enables a grain-to-grain analysis [Fig. 3(c)]. This excitation wavelength has been chosen because it is far from resonant with pure CuGaS<sub>2</sub>, CuGaSe<sub>2</sub>, and CuIn<sub>3</sub>Se<sub>5</sub> OVC phases<sup>25,32,35</sup> and has a penetration depth shorter than 100 nm. Two distinct Cu(In,Ga)Se<sub>2</sub> phases could be distinguished when measuring from the back side, one more Ga-rich and the other more In-rich, yielding peaks at 185 and 178 cm<sup>−1</sup>, respectively. For clarity, the individual measurements are divided into four groups depending on the dominating phase. The Ga-rich phase strongly dominates in groups 1 and 2, whereas the In-rich phase dominates the spectra in group 4. Group 3 regroups spectra where the two phases compete.

Complementary information on the variation of the bandgap from grain to grain can be obtained from cathodoluminescence spectroscopy (CL) in the scanning electron microscope (SEM). In

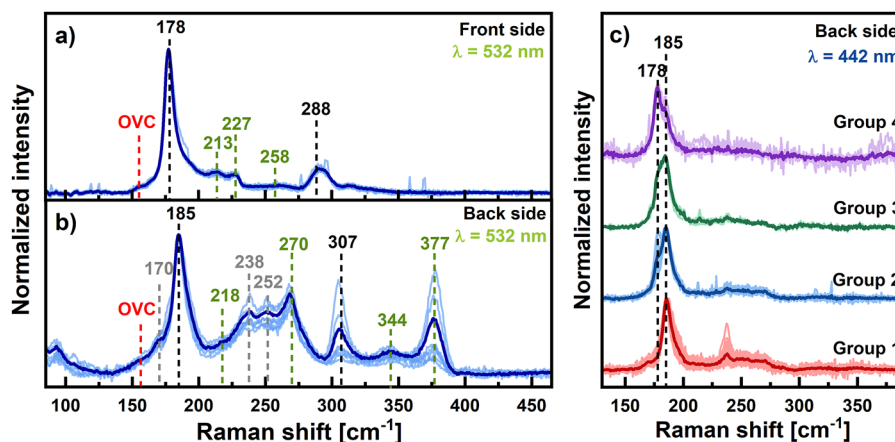


**FIG. 3.** Typical Raman spectra measured from (a) the front side before lift-off and (b) the back side after lift-off. A 532 nm wavelength laser is used as an excitation source. (c) Micro Raman on a 3 × 3 mm<sup>2</sup> area from the back side using a 442 nm wavelength laser as an excitation source. Individual measurements are ordered in groups 1–4, depending on the dominant peak. Pale lines in all figure parts are individual measurements taken in different positions and normalized to the peak related to Se–Se vibrations (178 and 185 cm<sup>−1</sup>, respectively). The darker lines are the resulting averaged spectra.

particular, CL is performed on the cross-section of an absorber similar to the one in Fig. 3 [red dot in Fig. 1(b)]. In each pixel, a spectrum is measured, making it possible to follow the evolution of the bandgap from the front surface down to the back side. Figure 4(a) shows a secondary electron (SE) cross-section image of the region where CL is performed. SE images are recorded under conditions optimized for CL imaging, which often have opposite imaging requirements and should be regarded only as a guide to follow from where the CL signal is coming from. Figure 4(b) reports the energy of the maximum of each individual spectrum. It is important to mention that this representation gives only a simple view of the bandgap energies, as some spectra, especially close to the back side, are too noisy to identify peaks. As the sample is slightly tilted, not only the cross section's emission is visible, but also the very front surface. The latter is dominated by a low gap phase with emission at about 1.13 eV (blue color). We relate this low gap phase to the low energy peak in the PL spectra, centered at 1.04 eV. Energy differences between the two measurement methods are attributed to the decreased quantum efficiency of the Si-camera used in CL at such low energies.

Considering individual line profiles from top to bottom along the cross-section of the film, we identify three scenarios, as indicated in Fig. 4(b) by the vertical lines: (i) a two phase region with an almost smooth transition from the front surface toward the back side; (ii) a three phase region with an almost smooth transition at the intermediate depth of the low gap and intermediate gap phases and with coexistence deeper in the intermediate and high gap phase; (iii) a two

phase region with coexistence in the middle of the film between the low gap and high gap phases. Individual spectra along the three lines are plotted in Fig. 4(c). In case (i), only one emission peak is detected, gradually increasing from 1.15 to 1.62 eV toward the back side. It should be noted, however, that in the transition region, the peak becomes wider than in the regions where clearly only one phase is detected. Cases (ii) and (iii) show distinct areas, indicating multiple phases. In case (ii), a gradual increase similar to the one from (i) is observed from 1.13 eV until 1.48 eV, but a sharp transition from 1.48 to 1.67 eV then occurs, as can be seen from the intermediate spectra where two peaks occur in the spectra. The low energy peak loses intensity as the higher energy one takes over. This abrupt transition from one recombination channel to another is observed in the colormap [Fig. 4(b)] as an abrupt change of color. The line profile (iii) is another example of such an abrupt change of recombination energy, happening however closer to the front surface, changing the dominant recombination from 1.28 to 1.61 eV. From a larger set of CL measurements performed on the same sample and on a second one with an additional sodium treatment (see Fig. S5 in supplementary material), it is seen that scenario (i) is not the most probable, but that generally, one or two abrupt transitions occur, indicating two or three discrete phases.

### C. Depth resolved investigation of the distinct interlaced phases

To support the hypothesis that the bulk of the absorber is made of interlaced distinct phases, depth resolved photoluminescence

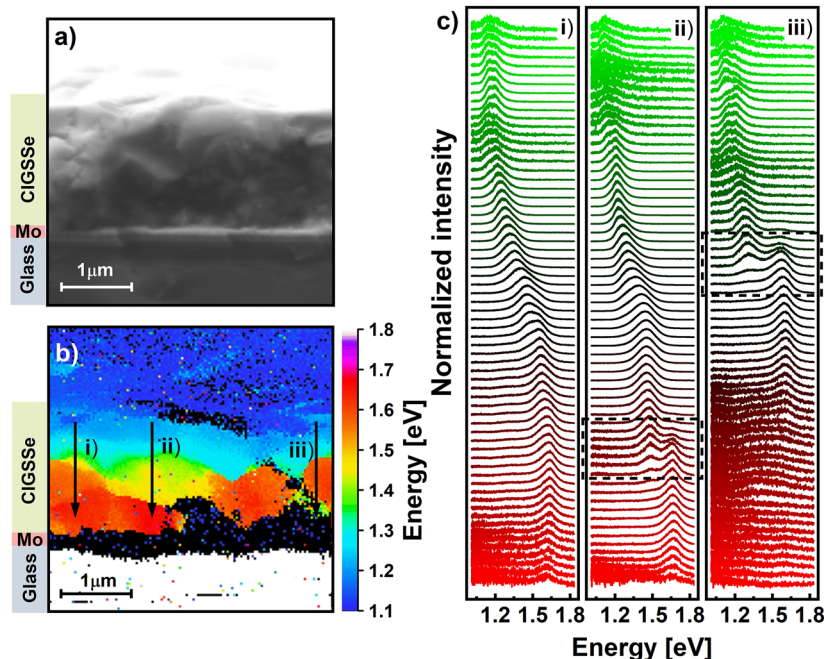


**FIG. 4.** (a) SE cross-section image of the region of interest where the CL is performed. (b) Colormap of the energy of the maximum of the CL emission. Orange-red corresponds to the high gap phase, green-yellow to the intermediate one, and blue-cyan to the low gap phase. The white region at the bottom is glass, and the black regions are either molybdenum (see left legend) or too noisy to identify peaks. (c) Individual spectra along the lines (i–iii) shown in (b). The peak in the transition region broadens compared to the region where only one peak is observed. The dashed boxes indicate the coexistence regions.

spectroscopy is performed after sequential etching of the absorber. Using the bromine etching routine described in the methods section, we gradually etch an absorber from region III [red dot in Fig. 1(b)] and measure the photoluminescence response at different depths throughout the thickness. Therefore, information about the depth distribution of the different phases can be accessed. Etching from the front and back sides has been performed, and the remaining thickness of the absorbed material is measured via an SEM cross-section. The etched surface generally presents an unequal roughness and, therefore, we estimate the error in the measurement of the thickness to be  $\pm 0.2 \mu\text{m}$ . Figure 5 shows the results from the two faces. These two measurements (front and back etching) are independent from each other and performed under different experimental conditions. Because of the lower signal from the back side, the excitation intensity for the measurement of the back side is set higher than for the front side. The spectra are all spectrally corrected but are not corrected in intensity. The measured PL flux is not absolute, but a relative comparison between the spectra within the same graph is possible.

After the first etching step from the front side, about 400 nm of material is etched, and the notch peak intensity increases by one order of magnitude. The low intensity of the non-etched absorber is attributed to the degraded surface after air exposure, which is a region of non-radiative recombinations.<sup>36,37</sup> We empirically notice that a buffered absorber remains stable for months, whereas a bare one oxidizes in a few hours in the air, resulting in a decrease in the PL intensity by up to two orders of magnitude. It should also be noted that even though there is a steep  $E_g$  increase at the very front

surface of the absorbers, the expected recombination when no etching is performed is still at the bandgap minimum due to carriers' diffusion. As more of the material is removed, we observe that the peak related to the notch recombination reduces in intensity and blueshifts slightly before disappearing entirely [see Fig. 5(a)]. This behavior correlates well with the bandgap profile shown in Fig. 5(c) and confirms that the dominant recombination occurs at the notch. As previously discussed, the GDOES profile should be considered in a qualitative way to address trends and not as offering absolute values, as we believe that not all the sulfur is in the bulk of the grains. On the other hand, before the notch peak disappears, the high energy peak, centered at 1.56 eV, is detected after 0.9  $\mu\text{m}$  of the absorber is etched and remains at constant energy until only 300 nm of material are left. This is in contradiction to the smooth profile indicated by GDOES and in agreement with the cathodoluminescence observations, which have already shown that some high bandgap material is present in the middle of the absorber and not solely at the back side.

To gain a better understanding of which contribution comes from what depth, we perform the etching (as well as the PL measurement) from the back side of the absorbers, thus conserving the notch at all times and removing only the back part [see Figs. 5(b) and 5(d)]. Therefore, no shift of the notch emission peak is observed, as expected. In a similar manner as from the front side, as more of the material is etched away, the high energy peak remains at constant energy. Additionally, it gradually loses intensity while the notch peak's intensity increases, confirming that the high gap phase is more present toward the back side of the absorber. Moreover, an additional PL peak at about 1.2 eV is detected at intermediate depth

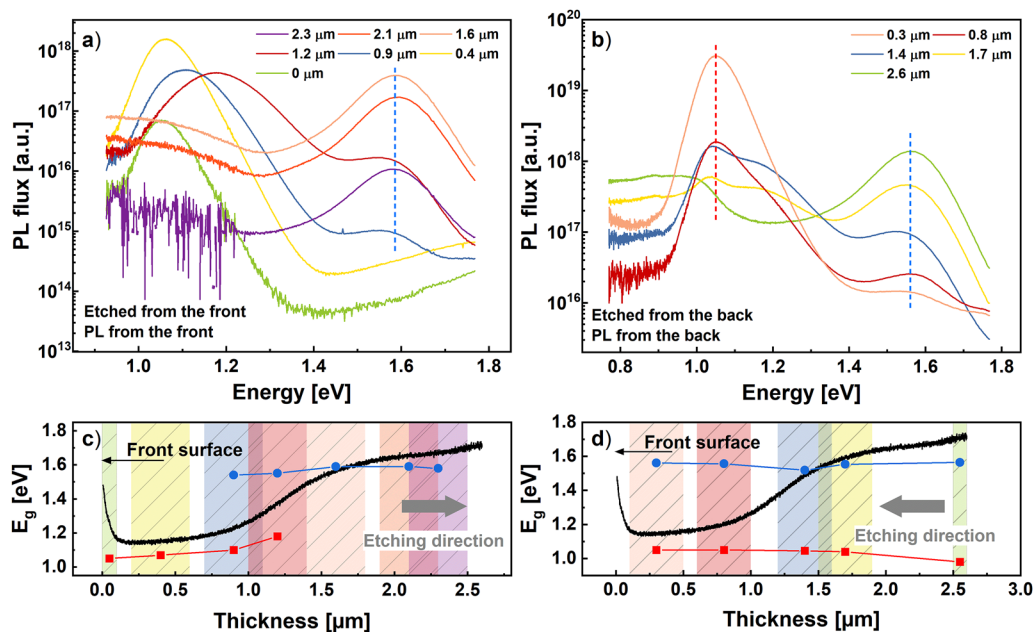


**FIG. 5.** Top: semi-log scale, non-absolute photoluminescence spectra at different depths after the absorber is gradually etched, from the front side (a) and from the back side (b). The legend indicates the depth relative to the front surface at which PL is performed (0  $\mu\text{m}$  corresponds to the front surface and 2.6  $\mu\text{m}$  to the back). The dashed lines represent the peaks' positions, also reported in (c) and (d). Bottom: bandgap profile determined from GDOES (black) and energies of the measured PL notch peak (red) and high energy peak (blue) at the different etching steps, from the front side (c) and back side (d). The colored bars indicate the etching depth, including errors.



in the absorber's bulk (at depths of 1.7 and 1.4  $\mu\text{m}$ ) from the back side, as can be seen in Fig. 5(b). We attribute this peak to a third phase of intermediate  $E_g$ , as already seen in CL spectroscopy [Fig. 4, line profile (ii)]. In addition, the broadening of the notch peak (at depths of 0.9 and 1.2  $\mu\text{m}$ ) when measuring from the front side is another indication of the presence of this phase. While cathodoluminescence provides information on the different phases present throughout the absorbers on a micrometer scale, photoluminescence collects signals from a few hundred grains at once. We, therefore, argue that depth resolved PL spectroscopy gives an average of the three scenarios discussed in Fig. 4, showing that mainly two or three individual phases with different GGI ratios are formed within the material. We propose in Fig. 6 a new model for the bandgap profile in such graded absorbers. According to GDOES measurements, a gradual increase from a low bandgap energy [green in Fig. 6(a)] toward a high bandgap energy (light red) is expected. However, as we demonstrated in this work, a situation as depicted in Fig. 6(b) seems more reasonable. A large density of high gap phase, the  $E_g$  of which is influenced by the GGI at the back side, forms close to the back contact of the absorber. Contrastingly, a low gap phase forms in high density toward the front side, generating the “notch” part of the absorber. In the bulk of the material, these two phases coexist at different densities, giving rise to an apparent gradient in the GDOES profile. In addition to the two main phases, a sparse phase of intermediate bandgap could be detected in the bulk, represented by the dark red color in Fig. 6(b). Finally, as observed by CL, some rare grains show a smooth  $E_g$  gradient, as highlighted in Fig. 6(b).

#### D. Effect of the back side luminescence on the radiative efficiency

Interestingly, as we etch from the back side past the steep Ga gradient and most of the high gap phase is removed (last etching step from the back side, at depth 0.3  $\mu\text{m}$ ), the notch peak's intensity increases by one order of magnitude. Its total integrated flux is  $3 \times 10^{18}$  photons/cm<sup>2</sup>/s. All other spectra in Fig. 5(b) have a similar total integrated flux of about  $3 \times 10^{17}$  photons/cm<sup>2</sup>/s. This strongly indicates that the non-radiative losses decrease when the back part is removed, i.e., that the back part of the absorber provides undesirable recombination paths that are detrimental to the absorber. A similar observation has been made based on carrier lifetime in graded CIGSe absorbers.<sup>38</sup> In fact, an increase of one order of magnitude in

PL intensity translates into an increase of  $\sim 60$  meV in quasi-Fermi level splitting, which gives an upper limit for the  $V_{OC}$  of the complete cell.<sup>9</sup> Among the undesirable recombination paths, a broad PL contribution centered at about 0.9 eV is detectable from the back side and from the front side after etching (see Figs. 2 and 5). Other chalcopyrite thin film studies reported PL emission at such low energy. Niki *et al.* observed a broad peak at about 0.85 eV in Cu-poor and Cu-rich CuInSe<sub>2</sub> films.<sup>39</sup> Mansfield *et al.* concluded that in standard Cu-poor Cu(In,Ga)Se<sub>2</sub>, a band-to-defect emission was detectable by PL spectroscopy at 0.79 eV.<sup>40</sup> More recently, Siebentritt *et al.* showed that a similar deep defect is also detected in sulfide chalcopyrites.<sup>41</sup> Spindler *et al.* reported a defect transition in Cu(In,Ga)Se<sub>2</sub> around 0.7–0.8 eV for high GGI and low GGI, respectively.<sup>42</sup> However, similarly to the observations in Ref. 39, they showed that the transition was more pronounced in Cu-rich films than in Cu-poor samples. They also discussed deep broad transitions around 1.10 and 1.24 eV in CuGaSe<sub>2</sub> at 10 K that they tentatively attributed to  $\text{Ga}_{\text{Cu}}$  and  $[\text{Ga}_{\text{Cu}}-2V_{\text{Cu}}]$ , respectively.<sup>43</sup> In the present work, the 0.9 eV defect emission may be a combination of the 0.8 and 1.10 eV defects. Furthermore, this defect emission disappears as the back part of the absorber is etched away, hinting that these defects are associated with the high gap phase, present in higher density at the back side. This defect disappearing could be the cause of the increase in PL intensity observed in Fig. 6(b) after the last etching step. Two additional absorbers [from region III, Fig. 1(b)] have been gradually etched from the back as well, but with shorter etching steps past the steep Ga gradient (see Fig. S6 in the supplementary material). It shows more clearly that the low energy PL peak intensity gradually increases as the back side is etched away. However, we cannot exclude the contribution of the interface between the low and high bandgap phases. When etching enough of the back side, less high bandgap material is left in the remaining absorber, reducing, therefore, the number of interfaces between low and high bandgap phases. This could, in turn, increase the PL intensity of the low energy peak.

To investigate the influence of the high gap phase on the radiative efficiency of the absorbers, we consider different CIGS<sub>se</sub> absorbers and measure for all of them absolute photoluminescence from both the front and back sides. On one hand, based on the measurements conducted on the front side, we extract the non-radiative losses as  $k_b T \times \ln(\text{PLQY})$ , where  $k_b$  is the Boltzmann constant,  $T$  is the temperature of the measurement, and PLQY is the photoluminescence quantum yield. On the other hand, based on the measurements from the back side, we determine the relative contribution of the high energy peak to the notch peak. In other words, we calculate the ratio of the integrated fluxes of the high energy peak and of the notch peak, referred to as the “peaks ratio” in Fig. 7.

Non-radiative losses through Shockley-Read-Hall recombination have a direct impact on the PLQY. As a consequence, both quasi-Fermi level splitting and  $V_{OC}$  are reduced by the same quantity,  $kT \ln(\text{PLQY})$ .<sup>24</sup> Based on an absolute PL investigation of absorbers, it is, therefore, possible to predict the losses in the device's performance. A linear relation between the non-radiative losses and the peaks ratio is obtained, demonstrating the negative impact of the high gap phase on the device's performance. We show that high non-radiative losses are associated with a high peak ratio and conclude from the fit that decreasing the amount of the high gap phase could reduce these losses by up to 180 meV.

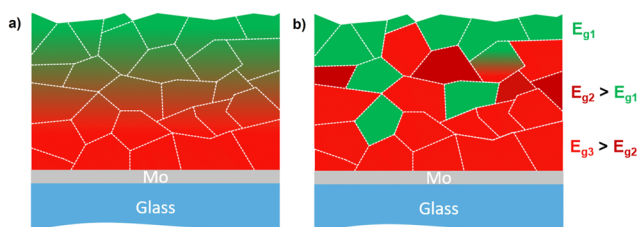


**FIG. 6.** Model for gallium gradient as suggested from the GDOES profile (a) and as proposed in this work based on other techniques (b). Green indicates a low bandgap phase ( $E_{g1}$ ), dark red is an intermediate bandgap phase ( $E_{g2}$ ), and light red is a high bandgap phase ( $E_{g3}$ ).

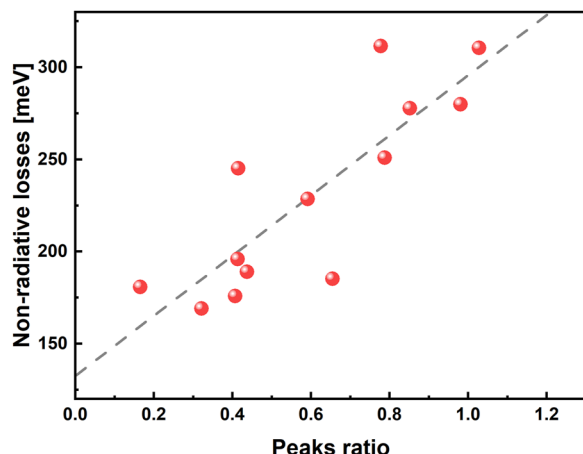


**FIG. 7.** Non-radiative losses vs peaks ratio for different CIGS<sub>Se</sub> absorbers. The peaks ratio is calculated as the ratio of the integrated PL fluxes of the high energy peak and of the low energy peak from measurements from the back side. The dashed line is a linear fit to the data.

#### IV. CONCLUSION

We demonstrated that the back side of graded Cu(In,Ga)(S,Se)<sub>2</sub> absorbers is a source of non-radiative recombination and, therefore, a limiting parameter for cells' performances. Depth resolved photoluminescence spectroscopy revealed that two main radiative recombination paths compete: one at about 1.04 eV, corresponding to recombination in the low gap phase, and one around 1.56 eV, attributed to recombination in the high gap phase. At intermediate depth into the bulk of the absorber, a third recombination path can sometimes be detected, indicating the presence of a sparse phase of the bandgap around 1.2 eV. Raman and cathodoluminescence spectroscopy confirm the formation of multiple phases and locate the low (high) bandgap phase close to the front (back) side. We propose that the bandgap gradient in graded absorbers is not a gradual increase from the front side toward the back side but rather that two main phases of low and high bandgap form, with the low gap phase predominantly near the front and the high gap phase predominantly near the back. The interlacing of these two phases in the bulk of the material produces the apparent gradient one can measure with GDOES.

In addition, we detect a broad defect band centered around 0.9 eV inside the high gap phase. We tentatively propose, as an origin, a combination of deep defects, one around 0.8 eV, commonly observed in selenide and sulfide chalcopyrites, and another one around 1.1 eV, as detected in CGSe. By etching the back side of the absorber until most of the high gap phase is removed, we measured a strong increase of one order of magnitude in the PL intensity of the notch peak, which translates into an increase of 60 meV in quasi-Fermi level splitting. Furthermore, we find a linear relation between the non-radiative voltage losses and the contribution of the high energy PL peak, highlighting the detrimental effect of the high gap phase. A decrease in the non-radiative losses of up to 180 meV could be expected by reducing the amount of the high gap phase.

#### SUPPLEMENTARY MATERIAL

See the supplementary material for complementary PL, CL, and Raman data as indicated in the text and details on bandgap determination based on different measurement methods.

#### ACKNOWLEDGMENTS

This work has been supported by Avancis, Germany, in the framework of the POLCA project and by EPSRC in the framework of the REACH project (No. EP/V029231/1), which are gratefully acknowledged. Authors from IREC belong to the MNT-Solar Consolidated Research Group of the "Generalitat de Catalunya" (Ref. No. 2021 SGR 01286) and are grateful to European Regional Development Funds (ERDF, FEDER Programa Competitivitat de Catalunya 2007–2013). M.G. acknowledges the financial support from the Spanish Ministry of Science, Innovation and Universities within the Juan de la Cierva fellowship (No. IJC2018-038199-I).

#### AUTHOR DECLARATIONS

##### Conflict of Interest

The authors declare no conflict of interest.

#### Author Contributions

**Aubin J.C. M. Prot:** Conceptualization (equal); Data curation (lead); Formal analysis (lead); Investigation (lead); Methodology (equal); Visualization (lead); Writing – original draft (lead); Writing – review & editing (lead). **Michele Melchiorre:** Formal analysis (supporting); Investigation (supporting). **Felix Dingwell:** Investigation (supporting); Writing – review & editing (supporting). **Anastasia Zelenina:** Data curation (equal); Formal analysis (equal); Investigation (equal); Methodology (equal); Resources (equal). **Hossam Elanzeery:** Data curation (equal); Formal analysis (equal); Investigation (equal); Methodology (equal); Resources (equal); Writing – review & editing (equal). **Alberto Lomuscio:** Data curation (equal); Formal analysis (equal); Investigation (equal); Methodology (equal); Resources (equal); Writing – review & editing (equal). **Thomas Dalibor:** Formal analysis (equal); Funding acquisition (lead); Resources (equal); Writing – review & editing (equal). **Maxim Guc:** Data curation (equal); Formal analysis (equal); Investigation (equal); Writing – review & editing (equal). **Robert Fonoll-Rubio:** Data curation (equal); Formal analysis (equal); Investigation (equal); Writing – review & editing (equal). **Victor Izquierdo-Roca:** Formal analysis (equal). **Gunnar Kusch:** Data curation (equal); Formal analysis (lead); Investigation (lead); Writing – review & editing (equal). **Rachel A. Oliver:** Conceptualization (lead); Formal analysis (equal); Funding acquisition (lead); Writing – review & editing (equal). **Susanne Siebentritt:** Conceptualization (lead); Formal analysis (equal); Funding acquisition (equal); Methodology (equal); Supervision (lead); Writing – review & editing (equal).

#### DATA AVAILABILITY

The data that support the findings of this study are openly available in Zenodo at <https://doi.org/10.5281/zenodo.8017507>.

## REFERENCES

- <sup>1</sup> Press release: New world record for thin-film modules (2023).
- <sup>2</sup> NREL, Best research-cell efficiencies (2023).
- <sup>3</sup> M. Nakamura, K. Yamaguchi, Y. Kimoto, Y. Yasaki, T. Kato, and H. Sugimoto, "Cd-free Cu(In,Ga)(Se,S)<sub>2</sub> thin-film solar cell with record efficiency of 23.35%," *IEEE J. Photovoltaics* **9**(6), 1863–1867 (2019).
- <sup>4</sup> M. A. Contreras, J. Tuttle, A. Gabor, A. Tennant, K. Ramanathan, S. Asher, A. Franz, J. Keane, L. Wang, and R. Noufi, "High efficiency graded bandgap thin-film polycrystalline Cu(In,Ga)Se<sub>2</sub>-based solar cells," *Sol. Energy Mater. Sol. Cells* **41–42**, 231–246 (1996).
- <sup>5</sup> M. Bodegård, O. Lundberg, J. Malmstrom, L. Stolt, and A. Rockett, "High voltage Cu(In,Ga)Se, devices with Ga-profiling fabricated using co-evaporation," in *Conference Record of the Twenty-Eighth IEEE Photovoltaic Specialists Conference* (IEEE, 2000).
- <sup>6</sup> A. M. Gabor, J. R. Tuttle, M. H. Bode, A. Franz, A. L. Tennant, M. A. Contreras, R. Noufi, D. G. Jensen, and A. M. Hermann, "Band-gap engineering in Cu(In,Ga)Se<sub>2</sub> thin films grown from (In,Ga)<sub>2</sub>Se<sub>3</sub> precursors," *Sol. Energy Mater. Sol. Cells* **41–42**, 247–260 (1996).
- <sup>7</sup> T. Wang, F. Ehre, T. P. Weiss, B. Veith-Wolf, V. Titova, N. Valle, M. Melchiorre, O. Ramirez, J. Schmidt, and S. Siebentritt, "Diode factor in solar cells with metastable defects and back contact recombination," *Adv. Energy Mater.* **12**(44), 2202076 (2022).
- <sup>8</sup> W. Shockley and H. J. Queisser, "Detailed balance limit of efficiency of p-n junction solar cells," *J. Appl. Phys.* **32**(3), 510–519 (1961).
- <sup>9</sup> S. Siebentritt, T. P. Weiss, M. Sood, M. H. Wolter, A. Lomuscio, and O. Ramirez, "How photoluminescence can predict the efficiency of solar cells," *J. Phys.: Mater.* **4**(4), 042010 (2021).
- <sup>10</sup> M. A. Green and A. W. Y. Ho-Baillie, "Pushing to the limit: Radiative efficiencies of recent mainstream and emerging solar cells," *ACS Energy Lett.* **4**(7), 1639–1644 (2019).
- <sup>11</sup> J. Palm, T. Dalibor, R. Lechner, S. Pohlner, R. Verma, R. Dietmüller, A. Heiß, H. Vogt, and F. Karg, in 29th European Photovoltaic Solar Energy Conference and Exhibition, 2014.
- <sup>12</sup> V. Probst, W. Stetter, W. Riedl, H. Vogt, M. Wendl, H. Calwer, S. Zweigart, K. D. Ufert, B. Freienstein, H. Cerva, and F. H. Karg, "Rapid CIS-process for high efficiency PV-modules: Development towards large area processing," *Thin Solid Films* **387**(1–2), 262–267 (2001).
- <sup>13</sup> M. H. Wolter, B. Bissig, E. Avancini, R. Carron, S. Buecheler, P. Jackson, and S. Siebentritt, "Influence of sodium and rubidium postdeposition treatment on the quasi-fermi level splitting of Cu(In,Ga)Se<sub>2</sub> thin films," *IEEE J. Photovoltaics* **8**(5), 1320–1325 (2018).
- <sup>14</sup> S. Lange, F. Giesl, V. Naumann, C. Hagendorf, and P. Eraerds, "Exfoliation methods for compositional and electronic characterization of interfacial Mo(Se<sub>x</sub>S<sub>y</sub>) in Cu(In,Ga)(Se,S)<sub>2</sub> solar cells by X-ray and UV photoelectron spectroscopy," *Surf. Interface Anal.* **54**, 688 (2022).
- <sup>15</sup> L. Weinhardt, O. Fuchs, A. Peter, E. Umbach, C. Heske, J. Reichardt, M. Bär, I. Laueremann, I. Kötschau, A. Grimm, S. Sokoll, M. C. Lux-Steiner, T. P. Niesen, S. Visbeck, and F. Karg, "Spectroscopic investigation of the deeply buried Cu(In,Ga)(S,Se)<sub>2</sub>/Mo interface in thin-film solar cells," *J. Chem. Phys.* **124**(7), 074705 (2006).
- <sup>16</sup> R. Scheer and H.-J. Lewerenz, "Formation of secondary phases in evaporated CuInS<sub>2</sub> thin films: A surface analytical study," *J. Vac. Sci. Technol., A* **13**(4), 1924–1929 (1995).
- <sup>17</sup> J. Lähnemann, J. F. Orri, E. Prestat, D. N. Johnstone, and N. Tappy, *LumiSpy/lumispy: v0.2.1* (2022).
- <sup>18</sup> M. Bär, W. Böhne, J. Röhrich, E. Strub, S. Lindner, M. C. Lux-Steiner, C. H. Fischer, T. P. Niesen, and F. Karg, "Determination of the band gap depth profile of the p-ternary Cu(In<sub>1-x</sub>Ga<sub>x</sub>)(S<sub>y</sub>Se<sub>1-y</sub>)<sub>2</sub> chalcopyrite from its composition gradient," *J. Appl. Phys.* **96**(7), 3857–3860 (2004).
- <sup>19</sup> J. Tauc, R. Grigorovici, and A. Vancu, "Optical properties and electronic structure of amorphous germanium," *Phys. Status Solidi* **15**, 627 (1966).
- <sup>20</sup> E. A. Davis and N. F. Mott, "Conduction in non-crystalline systems V. Conductivity, optical absorption and photoconductivity in amorphous semiconductors," *Philos. Mag.* **22**(179), 903–922 (1970).
- <sup>21</sup> R. Carron, C. Andres, E. Avancini, T. Feurer, S. Nishiwaki, S. Pisoni, F. Fu, M. Lingg, Y. E. Romanyuk, S. Buecheler, and A. N. Tiwari, "Bandgap of thin film solar cell absorbers: A comparison of various determination methods," *Thin Solid Films* **669**, 482–486 (2019).
- <sup>22</sup> J. Keller, R. Schlesiger, I. Riedel, J. Parisi, G. Schmitz, A. Avellan, and T. Dalibor, "Grain boundary investigations on sulfurized Cu(In,Ga)(S,Se)<sub>2</sub> solar cells using atom probe tomography," *Sol. Energy Mater. Sol. Cells* **117**, 592–598 (2013).
- <sup>23</sup> J. A. Curcio and C. C. Petty, "The near infrared absorption spectrum of liquid water," *J. Opt. Soc. Am.* **41**(5), 302–304 (1951).
- <sup>24</sup> S. Siebentritt, U. Rau, S. Gharabeiki, T. P. Weiss, A. Prot, T. Wang, D. Adeleye, M. Drahem, and A. Singh, "Photoluminescence assessment of materials for solar cell absorbers," *Faraday Discuss.* **239**, 112 (2022).
- <sup>25</sup> S. Sugai, "Resonant Raman scattering in CuGaS<sub>2</sub>," *J. Phys. Soc. Jpn.* **43**(2), 592–599 (1977).
- <sup>26</sup> W. Kauschke and M. Cardona, "Resonant Raman scattering in semiconductors," *Phys. Scr.* **T25**, 201–205 (1989).
- <sup>27</sup> F. Oliva, S. Kretschmar, D. Colomba, S. Tombolato, C. M. Ruiz, A. Redinger, E. Saucedo, C. Broussillou, T. G. de Monsabert, T. Unold, P. J. Dale, V. Izquierdo-Roca, and A. Pérez-Rodríguez, "Optical methodology for process monitoring of chalcopyrite photovoltaic technologies: Application to low cost Cu(In,Ga)(S,Se)<sub>2</sub> electrodeposition based processes," *Sol. Energy Mater. Sol. Cells* **158**, 168–183 (2016).
- <sup>28</sup> S. Y. Kim, M. S. Mina, J. Lee, and J. H. Kim, "Sulfur-alloying effects on Cu(In,Ga)(S,Se)<sub>2</sub> solar cell fabricated using aqueous spray pyrolysis," *ACS Appl. Mater. Interfaces* **11**(49), 45702–45708 (2019).
- <sup>29</sup> C. Insignares-Cuello, V. Izquierdo-Roca, J. López-García, L. Calvo-Barrio, E. Saucedo, S. Kretschmar, T. Unold, C. Broussillou, T. Goisard de Monsabert, V. Bermudez, and A. Pérez-Rodríguez, "Combined Raman scattering/photoluminescence analysis of Cu(In,Ga)Se<sub>2</sub> electrodeposited layers," *Sol. Energy* **103**, 89–95 (2014).
- <sup>30</sup> D. Nam, J. U. Lee, and H. Cheong, "Excitation energy dependent Raman spectrum of MoSe<sub>2</sub>," *Sci. Rep.* **5**, 17113 (2015).
- <sup>31</sup> T. Terasako, Y. Uno, T. Kariya, and S. Shirakata, "Structural and optical properties of In-rich Cu-In-Se polycrystalline thin films prepared by chemical spray pyrolysis," *Sol. Energy Mater. Sol. Cells* **90**(3), 262–275 (2006).
- <sup>32</sup> C. Insignares-Cuello, C. Broussillou, V. Bermúdez, E. Saucedo, A. Pérez-Rodríguez, and V. Izquierdo-Roca, "Raman scattering analysis of electrodeposited Cu(In,Ga)Se<sub>2</sub> solar cells: Impact of ordered vacancy compounds on cell efficiency," *Appl. Phys. Lett.* **105**(2), 021905 (2014).
- <sup>33</sup> S. B. Zhang, S.-H. Wei, and A. Zunger, "Stabilization of ternary compounds via ordered arrays of defect pairs," *Phys. Rev. Lett.* **78**, 4059 (1997).
- <sup>34</sup> K. Sato and H. Katayama-Yoshida, *AIP Conf. Proc.* **1583**, 150–155 (2014).
- <sup>35</sup> K. W. Kazuki Wakita, T. M. Takayuki Miyazaki, Y. K. Yasuhiro Kikuno, S. T. Souichi Takata, and N. Y. Nobuyuki Yamamoto, "Resonant Raman effect on a CuGaSe<sub>2</sub> crystal grown by the traveling heater method," *Jpn. J. Appl. Phys.* **38**(2R), 664–667 (1999).
- <sup>36</sup> D. Regesch, L. Gütay, J. K. Larsen, V. Deprédurand, D. Tanaka, Y. Aida, and S. Siebentritt, "Degradation and passivation of CuInSe<sub>2</sub>," *Appl. Phys. Lett.* **101**(11), 112108 (2012).
- <sup>37</sup> F. Babbe, L. Choubrac, and S. Siebentritt, "Quasi Fermi level splitting of Cu-rich and Cu-poor Cu(In,Ga)Se<sub>2</sub> absorber layers," *Appl. Phys. Lett.* **109**(8), 082105 (2016).
- <sup>38</sup> Y. H. Chang, R. Carron, M. Ochoa, C. Bozal-Ginesta, A. N. Tiwari, J. R. Durrant, and L. Steier, "Insights from transient absorption spectroscopy into electron dynamics along the Ga-gradient in Cu(In,Ga)Se<sub>2</sub> solar cells," *Adv. Energy Mater.* **11**(8), 2003446 (2021).
- <sup>39</sup> S. Niki, R. Suzuki, S. Ishibashi, T. Ohdaira, P. J. Fons, A. Yamada, H. Oyanagi, T. Wada, R. Kimura, and T. Nakada, "Anion vacancies in CuInSe<sub>2</sub>," *Thin Solid Films* **387**, 129–134 (2001).

<sup>40</sup>L. M. Mansfield, D. Kuciauskas, P. Dippo, J. V. Li, K. Bowers, B. To, C. Dehart, and K. Ramanathan, "Optoelectronic investigation of Sb-doped Cu(In,Ga)Se<sub>2</sub>," *IEEE J. Photovoltaics* **5**(6), 1769–1774 (2015).

<sup>41</sup>S. Siebentritt, A. Lomuscio, D. Adeleye, M. Sood, and A. Dwivedi, "Sulfide chalcopyrite solar cells—are they the same as selenides with a wider bandgap?," *Phys. Status Solidi RRL* **16**(8), 2200126 (2022).

<sup>42</sup>C. Spindler, F. Babbe, M. H. Wolter, F. Ehré, K. Santhosh, P. Hilgert, F. Werner, and S. Siebentritt, "Electronic defects in Cu(In,Ga)Se<sub>2</sub>: Towards a comprehensive model," *Phys. Rev. Mater.* **3**(9), 090302 (2019).

<sup>43</sup>C. Spindler, D. Regesch, and S. Siebentritt, "Revisiting radiative deep-level transitions in CuGaSe<sub>2</sub> by photoluminescence," *Appl. Phys. Lett.* **109**(3), 032105 (2016).